PAPER

Check for updates

1T-CrO$_2$ monolayer: a high-temperature Dirac half-metal for high-speed spintronics†

Shenda He,‡[a] Pan Zhou, ‡[a] Yi Yang,*[b] Wei Wang[a] and L. Z. Sun *[a]

Two-dimensional (2D) materials with complete spin-polarization, high-speed conduction electrons, large Curie temperatures and robust ferromagnetic ground states are desirable for spintronic applications. Based on first-principles calculations, we demonstrate that the 1T-CrO$_2$ monolayer is an intrinsic 3d ferromagnetic Dirac half metal (DHM) with two symmetry protected Dirac cones near the Fermi level. The Fermi velocities (3.21×10^5 m s^{-1} and 4.85×10^5 m s^{-1}) of the Dirac cones are in the same order as that of graphene, indicating its excellent transport properties. Its 2.48 eV half-metallic gap is large enough to prevent the spin-flip transition. Moreover, the two Dirac cones are robust against biaxial strain of up to ±4%. The robust ferromagnetism is mainly contributed by the 3d states of Cr and its Curie temperature is up to 507 K. Our results indicate that the ferromagnetic 1T-CrO$_2$ monolayer is a promising candidate for high temperature, high efficiency spintronics applications.

1 Introduction

Spintronics, through manipulating the spin degree of freedom in electronic devices, is a promising technology for next-generation electronics due to its low power consumption, high speed carrier transfer, high integration density and non-volatility.[1] Half-metals,[2] behaving as metals in one spin channel but as insulators or semiconductors in the opposite spin channel, have attracted great attention due to their direct application in spin filters, detectors and sensors for spintronics. Since the discovery and preparation of graphene,[3] hundreds of researchers, both experimental and theoretical, have been pursuing new 2D Dirac materials[2,4–6] due to their unique properties and tremendous potential applications, especially in nanoscale spintronics. There has been tremendous progress in searching for novel 2D materials with a broad range of electronic and optical properties,[3,7,8] unfortunately, most of them in the pristine form are nonmagnetic, which significantly hinders their application in spintronics.[9] Although magnetism can be introduced by dopants or defects,[10,11] these may destroy the Dirac state[12] and the long-range magnetic order was rarely observed. Hence, it is desirable to search for simple and intrinsic 2D materials with stoichiometric crystals which are ferromagnetic.

Subsequent to the establishment of the spin gapless semiconductors (SGSs) concept in spintronics,[13] Dirac half metals (DHMs) have been proposed based on a simple Kondo lattice model.[14] As for DHMs, a graphene-like Dirac state exists in one spin channel and a band gap opens in the other one, preventing the spin-flip of the spin-polarized Dirac state. Massless Dirac fermions derived from the linear dispersion of the Dirac cone show a substantially different nature from ordinary electrons, such as ballistic charge transport and enormously high carrier mobilities.[15,16] The coexistence of 100% spin polarization and massless Dirac fermions gives DHMs great potential for future nano-electronics, spintronics and optoelectronics. Moreover, the manipulation of both the charge and spin of the electrons only needs small external perturbations,[17] which meets the requirements of next-generation spintronic and electronic devices. Since the DHM concept was introduced,[14,18] several materials have been theoretically proposed to be DHMs,[9,10,19,20] such as heterostructures (CrO$_2$/TiO$_2$),[21] two-dimensional metal–organic frameworks (Mn(C$_6$H$_5$)$_3$, Mn-DCA and M$_3$C$_{12}$O$_{12}$),[1,22,23] honeycomb-Kagome lattices (VCl$_3$, C$_3$Ca$_2$ and Nb$_2$O$_3$)[12,24,25] and MXene materials (YN$_2$).[9,26] In comparison with TM doped 2D materials, one of the most intriguing merits of DHMs is their potentially high working temperature due to the intrinsic exchange interactions. For example, the Curie temperatures of YN$_2$ monolayers are up to 392 K, giving hope for their practical applications.[26] The high working temperatures of DHMs makes them a promising platform for the emerging area of spintronics devices with high Fermi velocities. However, until now, DHMs have rarely been predicted and, consequently, the realization and observation of intrinsic DHMs in experiments are still challenging. Thus, exploring DHM materials, particularly

[a] Hunan Provincial Key Laboratory of Thin Film Materials and Devices, School of Materials Science and Engineering, Xiangtan University, Xiangtan, 411105, China. E-mail: zhoupan71234@xtu.edu.cn; lzsun@xtu.edu.cn

[b] School of Materials Science and Engineering, Xiangtan University, Xiangtan, 411105, China. E-mail: yangyi@xtu.edu.cn

† Electronic supplementary information (ESI) available. See DOI: 10.1039/d0na00884b

‡ These authors contributed equally to this work.

DHMs with high Curie temperatures, is crucial to promote the development of spintronic devices.

In this work, using the first-principles method, we find that the 1T-CrO$_2$ monolayer is an intrinsic ferromagnetic DHM with a high Curie temperature of 507 K. When spin–orbit coupling is not considered, two spin-polarized Dirac cones are located at the high symmetry point K and the high symmetry line Γ–K, which endows the monolayer with interesting properties and potential applications in spintronics. The Fermi velocities, v_f, of the two Dirac cones (3.21×10^5 m s^{-1} and 4.85×10^5 m s^{-1}) are in the same order as those of graphene (9.5×10^5 m s^{-1}) and YN$_2$ (3.74×10^5 m s^{-1}),[9,27] which reveals the great carrier mobility of the monolayer. Moreover, the Dirac cones are protected by rotation symmetry and are robust under biaxial strain of up to ±4%. When considering the SOC, a small band gap opens for the two Dirac cones, however, this can be ignored at room temperature. Our results indicate that the 1T-CrO$_2$ monolayer is a promising DHM candidate for spintronics with a high Curie temperature.

2 Computational methods

The first-principles calculations were performed with the Vienna *ab initio* simulation package (VASP).[28,29] The projector-augmented-wave (PAW) potential was adopted to describe the interactions between the nucleus and the electrons. The generalized gradient approximation (GGA) of Perdew–Burke–Ernzerhof (PBE) was used for the exchange–correlation functional,[30] and the hybrid functional HSE06 (ref. 31) was used to validate the results obtained with PBE. The spin–orbit coupling effect was also taken into account as part of our calculations.[30,32] The cutoff energy was set to 520 eV, and the energetic and force convergence criteria were set as 10^{-6} eV and 10^{-2} eV, respectively. A $11 \times 11 \times 1$ Γ-centered Monkhorst–Pack K-sampling mesh was used for integration in the Brillouin zone (BZ). The atomic positions and the lattice constants were fully optimized by the conjugate gradient algorithm. A vacuum region of 20 Å was used to avoid interactions between neighboring periodic images of the monolayer. To confirm the dynamic stability of the 1T-CrO$_2$ monolayer, phonon spectra were obtained using the finite displacement method implemented in the CASTEP package[33] in Materials Studio software. Ultrasoft pseudopotentials were used, and the energy cutoff and SCF tolerance were set at 500 eV and 5×10^{-7} eV per atom, respectively. The cutoff radius was set at 5.0 Å, which means that a $4 \times 4 \times 1$ supercell was employed. The Monkhorst–Pack grid and separation of dispersion were set at the fine-level. To study the thermal stability of the 1T-CrO$_2$ monolayer, *ab initio* molecular dynamics (AIMD) simulations at 300 K for 6 ps were performed. Furthermore, to account for the localized 3d orbitals of the TM atoms more accurately, the Hubbard U correction was employed within the rotationally invariant DFT + U approach proposed by Dudarev *et al.*,[34] where only the $U_{eff} = U - J$ value is meaningful instead of the individual U and J values. We chose a broad range of U_{eff} values (0 ~ 5 eV) to allow a detailed examination of the effects of electronic correlation on the electronic structure of the system. The magnetic anisotropy energy (MAE) is defined as

the difference of the energies corresponding to the in-plane axis and out-of-plane axis. To obtain the magnetic anisotropy energy (MAE), noncollinear non-self-consistent calculations with SOC were performed.

3 Results and discussions

3.1 Structure and stability of the 1T-CrO$_2$ monolayer

Fig. 1(a) presents the top and side views of the 1T-CrO$_2$ monolayer, which contains one chromium (Cr) atom and two oxygen (O) atoms per unit cell, and the Cr atom is sandwiched into the two staggered O atomic layers. The space group of the monolayer is $P\bar{3}m1(D_{3d}^3$, no. 164). The lattice constants of 1T-CrO$_2$ are $a = b = 2.89$ Å and the bond length between neighbouring Cr and O atoms is 1.92 Å. To prove the stability of the monolayer, we calculate the energies under different strains and the results are presented in Fig. 1(c). The percentage strain is defined as $\varepsilon = (a_1 - a_0)/a_0$, where a_0 and a_1 are the lattice constants without or with strain, respectively. We find that the pristine 1T-CrO$_2$ is located at the energy extremum and it is stable under strain. Moreover, by distorting the 1T-CrO$_2$ monolayer, we can obtain a stable 1T$_d$-phase of CrO$_2$ with a ferromagnetic magnetic ground state. However, its average energy is higher than that of 1T-CrO$_2$. Therefore, we can conclude that the 1T phase is more stable than the 1T$_d$ phase for 2D CrO$_2$. The charge transfer between Cr and O atoms was investigated by Bader charge population analysis.[35] The results show that each O atom gets an average of 0.88e from the Cr atom, which indicates the ionic–covalent characteristic of the Cr–O bonds. To evaluate the energy stability of the 1T-CrO$_2$ monolayer, its cohesive energy $E_c(CrO_2)$ and formation energy $E_f(CrO_2)$ were obtained with the following formulae:

$$E_c(CrO_2) = \frac{E_s(Cr) + 2E_s(O) - E_t(CrO_2)}{3} \quad (1)$$

and

$$E_f(CrO_2) = \frac{E_t(CrO_2) - E_b(Cr) - 2E_b(O)}{3} \quad (2)$$

where $E_t(CrO_2)$ denotes the total energy of CrO$_2$ per unit cell, $E_s(Cr)$ and $E_s(O)$ are the energies of single Cr and O atoms, respectively, and $E_b(Cr)$ and $E_b(O)$ are the binding energies of each atom in pure chromium metal (body center cubic) and oxygen, respectively. The cohesive energy of the 1T-CrO$_2$ monolayer is 5.69 eV per atom, which is smaller than that of 2D graphene (7.86 eV per atom)[36] but larger than those of 1T-ZrSe$_2$ (5.35 eV per atom),[37] 1T-YN$_2$ (4.28 eV per atom)[9] and silicene (3.71 eV per atom).[38] The formation energy of the 1T-CrO$_2$ monolayer is $E_f(CrO_2) = -1.78$ eV per atom, and the negative value of E_f reveals that it can be synthesized from elemental Cr and O. To investigate the dynamic stability of the 1T-CrO$_2$ monolayer, the phonon spectra were calculated with a $4 \times 4 \times 1$ supercell using the CASTEP package,[33] and the results are presented in Fig. 1(b). The absence of imaginary frequencies reveals that the 1T-CrO$_2$ monolayer is dynamically stable. In addition, it is clearly indicated that the dispersion of the ZA mode around Γ is distinguished from the LA and TA modes,
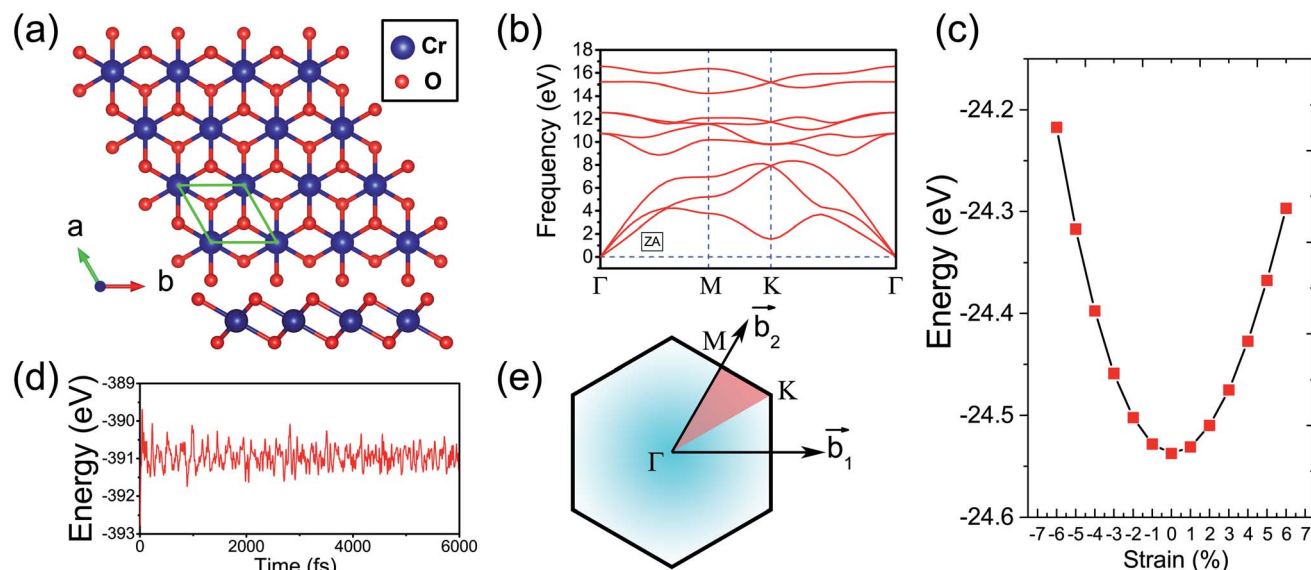
Fig. 1 (a) Top and side views of the 1T-CrO$_2$ monolayer. (b) Phonon dispersion curves of the 1T-CrO$_2$ monolayer. (c) Total energy of the unit cell as a function of strain. (d) Total potential energy fluctuation during molecular dynamics simulations at 300 K for 6 ps for the 1T-CrO$_2$ monolayer. (e) First Brillouin zone of the 1T-CrO$_2$ monolayer with the reciprocal lattice vectors $\vec{b_1}$ and $\vec{b_2}$.

which is very similar to the 1T phase of other two-dimensional materials, such as 1T-HfO$_2$,[39] 1T-ZrSe$_2$[40] and 1T-HfTe$_2$.[41] To analyze the mechanical stability, we calculated the linear elastic constants and the results with Voigt notation[42] are C$_{11}$ = 18.69 Gpa nm, C$_{22}$ = 18.53 Gpa nm, C$_{12}$ = 9.25 Gpa nm and C$_{44}$ = 4.59 Gpa nm. We can see that the elastic constants satisfy the Born-Huang criteria well[43] (C$_{11}$C$_{22}$–C$_{12}^2$ > 0 and C$_{44}$ > 0), which suggests the mechanical stability of the 1T-CrO$_2$ monolayer. Moreover, *ab initio* molecular dynamics (AIMD) simulations were carried out for 6 ps (with a time step of 1 fs) at 300 K and 600 K using a 4 × 4 × 1 supercell. The snapshots (the results can be found in Fig. S1 in the ESI†) and evolution of the energies as a function of time (see Fig. 1(d) and S1(c)†) reveal that 1T-CrO$_2$ is preserved well under these temperatures.

3.2 Magnetic ordering

3d transition metal Cr is included in 1T-CrO$_2$ and its preferential magnetic ground state firstly needs to be confirmed. As shown in Fig. 2, the antiferromagnetic (AFM) and ferromagnetic

(FM) configurations are presented for the supercell of 2 × 2 × 1. The energy of the FM configuration is 0.144 eV per Cr atom lower than that of the AFM one, indicating the ferromagnetic ground state of the 1T-CrO$_2$ monolayer. The integration of the spin-polarized electronic density around the Cr atoms shows that the magnetic moment of each Cr atom is 2 μ$_B$, corresponding to the d$^{1\downarrow3\uparrow}$ spin configuration of Cr^{2+}.

The magnetic exchange of the 1T-CrO$_2$ monolayer can be explained by the Goodenough–Kanamori–Anderson (GKA) formalism.[44–46] According to the GKA formalism, the magnetic properties are determined by two distinct exchange mechanisms: the direct exchange between two Cr atoms, and the superexchange interaction of Cr–O–Cr chains. Since the angle of Cr–O–Cr is nearly 90° (97.61°), and the distance of two Cr^{2+} cations is 2.89 Å, as shown in Fig. 3(a), the direct AFM exchange interactions are weak and the majority exchange mechanism is the superexchange interaction. The d-orbitals of Cr can only couple with the orthogonal p-orbitals of O, making it impossible for electrons on one of the d-orbitals of Cr to hop to the d-orbital of the nearest Cr atom. Therefore, the superexchange between the nearest Cr atoms is mediated by the middle O atom
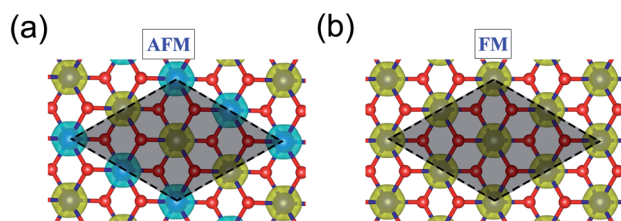

Fig. 2 The spatial distribution of spin-polarized electron density for the 1T-CrO$_2$ monolayer in the AFM (a) and FM (b) states. Yellow and blue represent the spin-up and spin-down charge densities, respectively. The isosurface is 0.03 e Å^{-3} and the gray area marks the AFM and FM cells that we used.
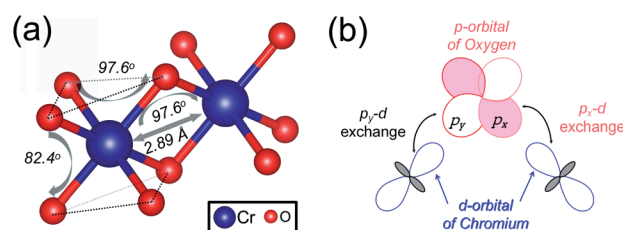

Fig. 3 (a) The structural parameters of the 1T-CrO$_2$ monolayer and the angle of Cr–O–Cr. (b) Illustration of the superexchange mechanism in 1T-CrO$_2$.

that forms a bridge between the two Cr atoms. It is worth noting that the p-orbitals which mediate the hopping of the two d-orbitals of the Cr atoms are the p_x and p_y orbitals of the O atoms, as shown in Fig. 3(b). The energy of the system depends on the relative spin orientation of the d and p states. According to Hund's rule, the O atoms tend to be triplet, namely the spin orientations of the p_x and p_y orbitals are parallel, which means that the d state hopping electrons of the two Cr atoms are also parallel to each other. In this case, the superexchange of the system produces the FM ordering for the 1T-CrO$_2$ monolayer. The magnetic anisotropy of the 1T-CrO$_2$ monolayer induced by SOC[47] is an important property related to its magnetic stability, which keeps the long-range magnetic ordering of the monolayer and counteracts thermal fluctuations.[48] We have performed noncollinear magnetic calculations to obtain the magnetic anisotropy energy (MEA) of the 1T-CrO$_2$ monolayer, and the results indicate that the easy magnetization axis is along the in-plane [100] direction.

3.3 Electronic properties and Curie temperature

Based on the ferromagnetic ground state of the 1T-CrO$_2$ monolayer proven above, the spin-resolved band structure without spin–orbit coupling (SOC) and the corresponding local density of states (LDOS) are shown in Fig. 4(a). The results indicate that there are two Dirac cones in the spin up channel located at the high symmetry point K (denoted as D_1) and the high symmetry line Γ–K (denoted as D_2). D_1 is rightly located at the K point and is similar to that of graphene and 1T-Na$_2$C.[27] Therefore, we expect that this cone is protected by C_3 rotation symmetry. For the cone of D_2, we find that only the C_2 rotation operator exists along the high symmetry line Γ–K (Fig. S2†). Further symmetry representation calculations reveal that the two crossing bands have opposite eigenvalues to the C_2 operator, which indicate D_2 is protected by the C_2 rotation symmetry. The energy levels of the two Dirac points are 0.194 eV (D_1) and 0.187 eV (D_2) higher than the Fermi level. The results show that the system has half metallic behaviour and the Dirac cones are 100% spin polarized. Moreover, the insulating spin-down channel shows a band gap of 2.48 eV, making the spin-up channel, which includes the spin-polarized Dirac cones, extremely pure and steady around the Fermi level. These characteristics are favorable for spintronics due to it meaning spin-flip is avoided.

According to the spin-resolved LDOS and orbital-resolved band structures shown in Fig. 4, we find that the band crossings are mainly contributed to by the d states of the Cr atoms. Furthermore, the v_f of the Dirac cones are 3.21×10^5 m s^{-1} (D_1) and 4.85×10^5 m s^{-1} (D_2), which are in the same order as that of graphene (9.5×10^5 m s^{-1}),[27] and in particular the v_f of D_2 is above half of that of graphene, implying the high electron mobility in the monolayer. The large gap of the insulating channel (spin-down), in combination with the pure and high electron mobility in the other channel (spin-up) of the 1T-CrO$_2$ monolayer, can filter the current into a single spin channel effectively. These properties can be beneficial for the application of the 1T-CrO$_2$ monolayer in polarization optics and spintronics.[13] When considering the effect of SOC, the results shown in Fig. 4(b) indicate that the Dirac cones open negligible gaps of 17 meV (D_1) and 21 meV (D_2). The feature of the Dirac cones is still preserved due to the tiny gap induced by the SOC which can always be ignored with the thermal perturbation under room temperature.

Additionally, the calculated 2D Young's modulus is 140 N m^{-1}, which is lower than that of graphene (340 N m^{-1})[49] but higher than those of 2D MoS$_2$ (130 N m^{-1})[50] and 2D NiCl$_3$ (25 N m^{-1}).[20] According to the stress–strain diagram in Fig. S6,† we find that the stress suddenly changes at a strain of 20%. This indicates that 20% is the elastic limit of 2D CrO$_2$. That is to say that this material can keep its original stable structure when the strain is not beyond 20%. These results demonstrate that the effect of strain must be taken into consideration because it may influence the band structure of the monolayer. Therefore, we checked the stability of the DHM properties under external strain. The DHM states are still preserved under strain of up to ±4%, and the results can be found in Fig. S3 in the ESI,† indicating the robustness of the DHM properties of the 1T-CrO$_2$ monolayer with regards to external strain.
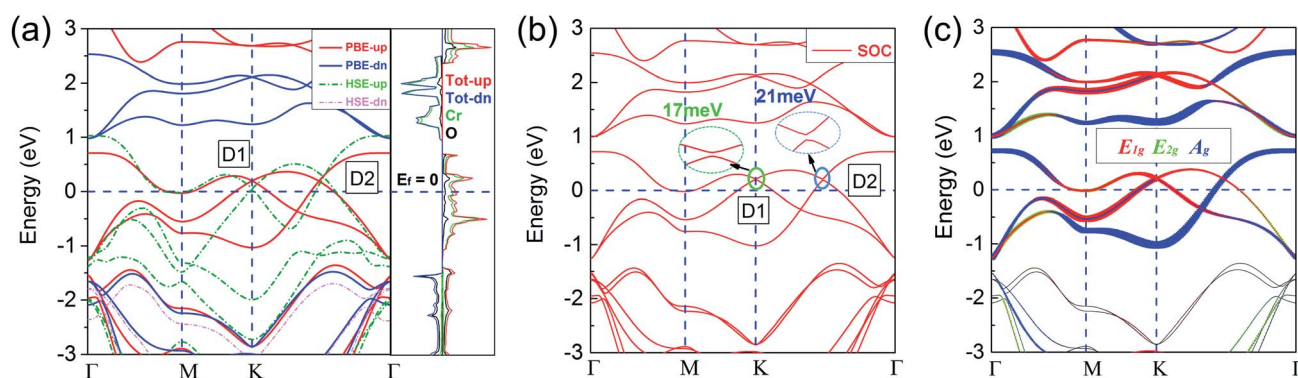

Fig. 4 (a) Spin-polarized band structures from PBE and HSE06. The red (green) and blue (pink) lines (dashed lines) represent the spin-up and spin-down channels calculated by PBE (HSE06), respectively. The spin-resolved local densities of states (LDOS) from PBE are also presented. (b) Band structure with SOC. The tiny band gaps of D_1 and D_2 are 17 meV and 21 meV, respectively. All Fermi levels are set to zero. (c) Under the trigonal crystal field of the O atoms, the d orbitals of the Cr atoms can be split into three groups: E_{1g}(d$_{x^2-y^2}$, d$_{xy}$), E_{2g}(d$_{xz}$, d$_{yz}$) and A_g(d$_{z^2}$).
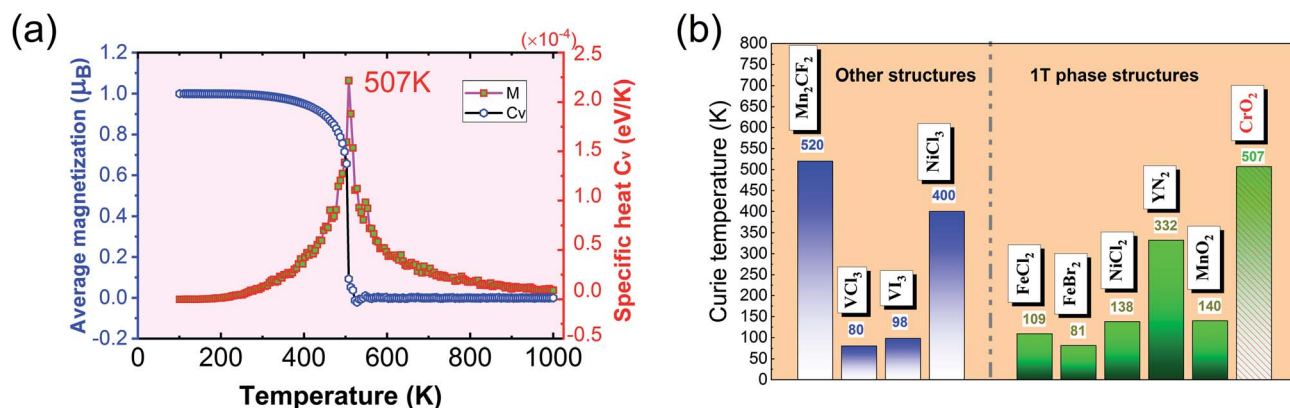
Fig. 5 (a) The average magnetic moment (blue) and specific heat (red) as functions of temperature. The two figures reveal that the T_c of 1T-CrO$_2$ is 507 K. (b) The comparison of the T_c of the 1T-CrO$_2$ monolayer with previously reported 2D transition metal compounds, where the green (blue) bars represent the 1T structured (other structured) monolayer similar to (different from) that of CrO$_2$.

For 3d transition metal compounds, the influence of correlation effects is significant. To estimate the correlation effects, the GGA + U method was used. Moreover, the cRPA[51] method was used to evaluate the Hubbard U. The calculated $U_{eff} = 2$ eV, which indicates that the electronic correlation of element Cr in the 1T-CrO$_2$ monolayer is weaker than that in the Cr$_2$O$_3$ bulk state ($U_{eff} = 3.6$ eV).[52] The band structure with Hubbard $U_{eff} = 2$ eV is presented in Fig. S4(b) in the ESI.† The results indicate that the Dirac cones are well preserved. Interestingly, the Hubbard U_{eff} enlarges the band gap of the spin-down channel to larger than 3 eV, which is favorable for avoiding the spin flip of the spin-up channel. Furthermore, we chose a broad range of values of U_{eff} from 0 eV to 5 eV to examine in detail the correlation effect on the electronic structure of the system, and the results are shown in Fig. S4 in the ESI.† The results show that the influence of the Hubbard U_{eff} on the electronics of the system, especially the Dirac cones, is negligible. The half-metallicity is well retained and the Dirac cone D_1 is close to Fermi level with the increase in the value of U_{eff}. Intriguingly, the band gap of the spin-down channel is enlarged with the increase in the value of U_{eff}. These results indicate that the DHM characteristics of the 1T-CrO$_2$ monolayer are robust to the on site Hubbard U_{eff} correction.

The Curie temperature (T_c) is one of the most important parameters to guarantee the magnetic ordering stability of the 1T-CrO$_2$ monolayer. Based on the energy difference ($\Delta E = 0.144$ eV) of the AFM and FM orderings, we can estimate the T_c from the mean-field approximation (MFA)[53] *via*

$$\frac{3}{2}K_B T_c^{MFA} = \Delta E \tag{3}$$

where K_B is the Boltzmann constant. The obtained T_c^{MFA} is 1114 K. As the MFA tends to overestimate the value of T_c,[9] we further perform Monte-Carlo (MC) simulations with the magnetic Ising model.[54] We use a 100×100 lattice to perform MC simulations and the periodic boundary condition is imposed. The numbers of steps at each temperature is set to 1×10^6. On each site, the spin magnetic moment is set to 2 μ_B. The spin Hamiltonian can be written as

$$H = -\sum_{\langle i,j \rangle} J S_i S_j \tag{4}$$

where the summation runs over all six nearest neighboring Cr sites and J is the nearest-neighboring exchange parameter, which is defined as

$$J = \frac{E_{AFM} - E_{FM}}{2ZS^2} \tag{5}$$

where $Z = 6$ is the number of nearest-neighboring Cr atoms in the 1T-CrO$_2$ monolayer and $E_{AFM(FM)}$ is the total energy per unit cell for the AFM (FM) state. To illustrate the effect of strain on the exchange constant J, we calculate the values of J with different biaxial strains and the detailed results are presented in the ESI.† We find no evident changes happening in the range of -5%–5% biaxial strain. The average magnetization M_{Avg} and specific heat C_v are defined by

$$M_{Avg} = \frac{1}{N} \sum_{i=1}^{N} (M_{up} - M_{dn}) \tag{6}$$

and

$$C_v = \frac{N(\langle H^2 \rangle - \langle H \rangle^2)}{K_B T^2}. \tag{7}$$

The calculated results of these at different temperatures are presented in Fig. 5. We find that the average magnetic moment suddenly decreases at around 507 K. At the same time, the specific heat C_v also reaches a sharp peak near this temperature. Both of these results reveal that the Curie temperature of CrO$_2$ is close to 507 K. This value share similar level with that of Mn$_2$CF$_2$ (ref. 55) and is higher than those of other transition metal compounds.[9,12,20,56,57] A detailed comparison can be found in Fig. 5(b). For a triangular system, the ratio of Curie temperatures between mean field and experiment is approximately equal to 0.61($T_c^{MFA}/T_c \approx 0.61$).[53] According to our results of $T_c^{MFA} = 1114$ K and $T_c = 507$ K, the ratio of these is 2.2, which is almost three times the empirical value. The high T_c of the 1T-

CrO$_2$ monolayer demonstrates that it is a potential candidate for future room temperature spintronics.

4 Conclusions

In the present work, we find that the 1T-CrO$_2$ monolayer is a stable DHM with a Curie temperature of 507 K. Its ferromagnetic ground state can be understood by the superexchange mechanism from the GKA rules. The large insulating gap (2.48 eV) of the opposite spin channel prevents the spin-flip transition happening between the two different channels. There are two spin-polarized Dirac cones at the high symmetry point K and along the high symmetry line K–Γ. The Fermi velocities of these two cones are in the same order as that of graphene. We expect the 1T-CrO$_2$ monolayer to be a promising platform for future high efficiency spintronic applications.

Conflicts of interest

There are no conflicts to declare.

Acknowledgements

Notes and references

1 X. Wang, T. Li, Z. Cheng, X.-L. Wang and H. Chen, *Appl. Phys. Rev.*, 2018, **5**, 041103.

2 R. A. de Groot, F. M. Mueller, P. G. v. Engen and K. H. J. Buschow, *Phys. Rev. Lett.*, 1983, **50**, 2024–2027.

3 K. S. Novoselov, A. K. Geim, S. V. Morozov, D. Jiang, Y. Zhang, S. V. Dubonos, I. V. Grigorieva and A. A. Firsov, *Science*, 2004, **306**, 666–669.

4 P. Dowben, *J. Phys.: Condens. Matter*, 2007, **19**, 310301.

5 K. W. Lee and C. E. Lee, *Adv. Mater.*, 2012, **24**, 2019–2023.

6 I. Galanakis and E. Saslogul, *Appl. Phys. Lett.*, 2011, **99**, 052509.

7 K. F. Mak, K. L. McGill, J. Park and P. L. McEuen, *Science*, 2014, **344**, 1489–1492.

8 Q. Sun, Y. Dai, Y. Ma, N. Yin, W. Wei, L. Yu and B. Huang, *2D Mater.*, 2016, **3**, 035017.

9 Z. Liu, J. Liu and J. Zhao, *Nano Res.*, 2017, **10**, 1972–1979.

10 Y. Li, D. West, H. Huang, J. Li, S. B. Zhang and W. Duan, *Phys. Rev. B: Condens. Matter Mater. Phys.*, 2015, **92**, 201403.

11 J. Červenka, M. Katsnelson and C. Flipse, *Nat. Phys.*, 2009, **5**, 840–844.

12 J. He, S. Ma, P. Lyu and P. Nachtigall, *J. Mater. Chem. C*, 2016, **4**, 2518–2526.

13 X. L. Wang, *Phys. Rev. Lett.*, 2008, **100**, 156404.

14 H. Ishizuka and Y. Motome, *Phys. Rev. Lett.*, 2012, **109**, 237207.

15 K. S. Novoselov, A. K. Geim, S. V. Morozov, D. Jiang, M. I. Katsnelson, I. V. Grigorieva, S. V. Dubonos and A. A. Firsov, *Nature*, 2005, **438**, 197–200.

16 S. V. Morozov, K. S. Novoselov, M. I. Katsnelson, F. Schedin, D. C. Elias, J. A. Jaszczak and A. K. Geim, *Phys. Rev. Lett.*, 2008, **100**, 016602.

17 X. Wang, *Natl. Sci. Rev.*, 2017, **4**, 252–257.

18 Y. Akagi and Y. Motome, *Phys. Rev. B: Condens. Matter Mater. Phys.*, 2015, **91**, 155132.

19 Y. Wang, S. Li, C. Zhang, S. Zhang, W. Ji, P. Li and P. Wang, *J. Mater. Chem. C*, 2018, **6**, 10284–10291.

20 J. He, X. Li, P. Lyu and P. Nachtigall, *Nanoscale*, 2017, **9**, 2246–2252.

21 T. Cai, X. Li, F. Wang, S. Ju, J. Feng and C. Gong, *Nano Lett.*, 2015, **15**, 6434–6439.

22 Y. Wang, W. Ji, C.-w. Zhang, P. Li, P. Wang, B. Kong, S. Li, S. Yan and K. Liang, *Appl. Phys. Lett.*, 2017, **110**, 233107.

23 M. Wu, Z. Wang, J. Liu, W. Li, H. Fu, L. Sun, X. Liu, M. Pan, H. Weng and M. Dincă, *2D Mater.*, 2016, **4**, 015015.

24 W. Ji, B. Zhang, S. Zhang, C. Zhang, M. Ding, P. Li and P. Wang, *J. Mater. Chem. C*, 2017, **5**, 8504–8508.

25 S. Zhang, C. Zhang, S. Zhang, W. Ji, P. Li, P. Wang, S. Li and S. Yan, *Phys. Rev. B*, 2017, **96**, 205433.

26 X. Kong, L. Li, O. Leenaerts, W. Wang, X. Liu and F. M. Peeters, *Nanoscale*, 2018, **10**, 8153–8161.

27 W. Ji, B. Zhang, S.-F. Zhang, C. Zhang, M. Ding, P. Wang and R. Zhang, *Nanoscale*, 2018, **10**, 13645–13651.

28 G. Kresse and J. Furthmüller, *Comput. Mater. Sci.*, 1996, **6**, 15–50.

29 G. Kresse and J. Furthmüller, *Phys. Rev. B: Condens. Matter Mater. Phys.*, 1996, **54**, 11169.

30 J. P. Perdew, K. Burke and M. Ernzerhof, *Phys. Rev. Lett.*, 1996, **77**, 3865.

31 A. V. Krukau, O. A. Vydrov, A. F. Izmaylov and G. E. Scuseria, *J. Chem. Phys.*, 2006, **125**, 224106.

32 P. E. Blöchl, *Phys. Rev. B: Condens. Matter Mater. Phys.*, 1994, **50**, 17953.

33 S. J. Clark, M. D. Segall, C. J. Pickard, P. J. Hasnip, M. J. Probert, K. Refson and M. Payne, *Z. Kristall.*, 2005, **220**, 567–570.

34 S. Dudarev, G. Botton, S. Savrasov, C. Humphreys and A. Sutton, *Phys. Rev. B: Condens. Matter Mater. Phys.*, 1998, **57**, 1505.

35 G. Henkelman, A. Arnaldsson and H. Jónsson, *Comput. Mater. Sci.*, 2006, **36**, 354–360.

36 Y. Han, K. C. Lai, A. Lii-Rosales, M. C. Tringides, J. W. Evans and P. A. Thiel, *Surf. Sci.*, 2019, **685**, 48–58.

37 G. Özbal, R. Senger, C. Sevik and H. Sevinçli, *Phys. Rev. B*, 2019, **100**, 085415.

38 L.-M. Yang, V. Bacic, I. A. Popov, A. I. Boldyrev, T. Heine, T. Frauenheim and E. Ganz, *J. Am. Chem. Soc.*, 2015, **137**, 2757–2762.

39 J. Weng and S.-P. Gao, *Phys. Chem. Chem. Phys.*, 2018, **20**, 26453–26462.

40 G. Özbal, R. T. Senger, C. Sevik and H. Sevinçli, *Phys. Rev. B*, 2019, **100**, 085415.

41 M. L. Adam and A. A. Bala, *Computational Condensed Matter*, 2021, **26**, e00527.

42 R. C. Andrew, R. E. Mapasha, A. M. Ukpong and N. Chetty, *Phys. Rev. B: Condens. Matter Mater. Phys.*, 2012, **85**, 125428.

43 M. Born and K. Huang, *Dynamical theory of crystal lattices*, Clarendon press, 1954.

44 J. B. Goodenough, *Phys. Rev.*, 1955, **100**, 564.

45 J. Kanamori, *J. Appl. Phys.*, 1960, **31**, S14–S23.

46 P. W. Anderson, *Phys. Rev.*, 1959, **115**, 2.

47 J. L. Lado and J. Fernández-Rossier, *2D Mater.*, 2017, **4**, 035002.

48 N. D. Mermin and H. Wagner, *Phys. Rev. Lett.*, 1966, **17**, 1133.

49 C. Lee, X. Wei, J. W. Kysar and J. Hone, *Science*, 2008, **321**, 385–388.

50 J. Jiang, Z. Qi, H. S. Park and T. Rabczuk, *Nanotechnology*, 2013, **24**, 435705.

51 B. Amadon, T. Applencourt and F. Bruneval, *Phys. Rev. B: Condens. Matter Mater. Phys.*, 2014, **89**, 125110.

52 S. Shi, A. L. Wysocki and K. D. Belashchenko, *Phys. Rev. B: Condens. Matter Mater. Phys.*, 2009, **79**, 104404.

53 N. W. Ashcroft, N. D. Mermin and D. Wei, *Solid State Physics*, Cengage Learning Asia Pte Limited, 2016.

54 J. Kotze, arXiv:0803.0217, 2008.

55 J. He, P. Lyu and P. Nachtigall, *J. Mater. Chem. C*, 2016, **4**, 11143–11149.

56 V. V. Kulish and W. Huang, *J. Mater. Chem. C*, 2017, **5**, 8734–8741.

57 M. Kan, J. Zhou, Q. Sun, Y. Kawazoe and P. Jena, *J. Phys. Chem. Lett.*, 2013, **4**, 3382–3386.